WILEY | Hindawi

Research Article

Study on the Failure Mechanism of Lower Cambrian Shale under Different Bedding Dips with Thermosolid Coupling

Wentao Wang [1], **Zhonghu Wu** [1,2,3] **Huailei Song** [1] **Hengtao Cui,**[1] **Yili Lou,**[1] **Motian Tang** [1] **and Hao Liu**[4]

[1]*College of Civil Engineering, Guizhou University, Guiyang 550025, China*
[2]*School of Qilu Transportation, Shandong University, Jinan 250002, China*
[3]*Geotechnical and Structural Engineering Research Center, Shandong University, Jinan 250061, China*
[4]*Mining College, Guizhou University, Guiyang, Guizhou 550025, China*

Correspondence should be addressed to Zhonghu Wu; wuzhonghugzu@163.com

To investigate the damage pattern and acoustic emission pattern of temperature on laminated shales, numerical experiments were carried out using the RFPA2D-Thermal numerical software under the effect of thermosolid coupling. During the tests, temperatures of 30°C, 60°C, and 90°C were controlled, and five sets of shales containing different laminar dips were numerically modeled at each temperature, with dips of 0°, 22.5°, 45°, 67.5°, and 90°. The test results show that (1) the increase in temperature reduced the linear elastic phase of the shale specimens in each group, with a significant reduction in the linear elastic phase of the shale at lamina dips of 22.5° and 45°. (2) The lamination effect decreased slightly as the temperature rose from 30°C to 60°C, and the most significant enhancement of the lamination effect on the shale occurred when the temperature reached 90°C. (3) The shale damage pattern is divided into five types (N, Λ, v, slanted I-type, and cluttered-type), in which the lamina effect is stronger for high-angle lamina dips, and the lamina surface has a strong dominant effect on the entire shale crack expansion. At a temperature of 90°C, the lamina effect and temperature effect of the shale reached their maximum at the same time, and the thermal and load stresses inside the shale acted together causing the shale to show a complex damage mode. (4) The fractal dimension was used to analyze the damage pattern of the shale. The larger the fractal dimension was, the greater the crack rate of the specimen. The fractal dimension curve was flatter at a temperature of 60°C, while at 90°C, the fractal dimension rose rapidly, indicating the most favorable crack expansion in the shale at a temperature of 90°C.

1. Introduction

As the first country to develop shale gas, the United States has succeeded in reducing natural gas consumption and has seen a gradual increase in natural gas exports, contributing to the optimization of the US energy system [1–5]. In recent years, with the massive depletion of conventional energy sources, there has been an urgent need for a new q-energy source that can replace natural gas and oil, which has led to strong interest in shale gas from all corners of the world [6–13].

Currently, the commonly used technology in shale gas exploitation is hydraulic fracturing technology. In hydraulic fracturing technology, a series of rock mechanic problems are involved [14–20]. Hence, exploring the mechanical ability of shale is of outstanding importance for the evolution of reformed shale gas reservoirs. Shale gas is stockpiled in shale pores containing shale gas under high ambient stress and high-temperature conditions. Therefore, the exploitation of shale gas always includes the coupling of stress and temperature fields [21–23].

Inhomogeneous bedding has attracted the attention of scholars for a long time, but the temperature impact on the mechanical properties of shale rocks has only gradually received attention since the 1970s. Therefore, domestic and foreign researchers have acquired successful outcomes regarding the effect of temperature on the mechanical properties of shale rocks. Lou et al. [24] used numerical modeling

experiments to probe the bedding effects of shale with different bedding dips and applied fractal dimensions to analyze the crack laws of shale. Wei et al. [25] created a thermal damage thermosolid coupling model, performed physical tests on granites, and found that the thermal effect caused changes in rock parameters thereby stimulating rock tensile-reduction damage. Zhou et al. [26] established compression, and the thermosolid coupling model of thermal expansion provided the thermosolid coupling equation for shale. Alm et al. [27] studied the effect of microcrack density on the elastic and mechanical properties of granite. After the granite was heated, the crack density of the rock was measured by scanning electron microscopy and other instruments, and finally, it was found that when the temperature exceeded 300°C, the crack density increased significantly. Lu et al. [28] carried out a large-scale triaxial compression test on shale. By controlling temperature variables, the relationship between temperature, peak strength of shale, Poisson's ratio, internal elastic modulus, and friction angle was found. Wang et al. [29] found that the fractality, connectivity and connectivity of parallel laminations were 1.31, 1.12, and 1.61 times higher than those of vertical ones by studying the coal rocks in the Fukang Mine area. Yao et al. [30] investigated the mechanical properties of outcrop shale under different laminar dip angles and found that the damage extension direction almost coincided with the laminar dip angle around 0~45°, and when the dip angle was 60~90°, only a small part of the fracture extension direction coincided with the laminar dip angle. Only a small part of the fracture extension direction coincides with the laminar dip angle.. Masri et al. [31] performed hydrostatic and conventional triaxial tests to explore the mechanical properties of the bedding angles of parallel and vertical bedding angles at different temperatures. As the temperature rose, the elastic modulus and compressive strength of the rock were weakened, but the overall deformation was strengthened. Gautam et al. [32] studied the deformation characteristics of sandstone at various temperatures. They observed that the stress-strain curve showed that sandstone underwent brittle deformation at 250°C, and plastic deformation occurred when the temperature exceeded 450°C. Ranjith et al. [33] performed uniaxial compression tests on Hawkesbury sandstone at different temperatures. The results showed that the maximum elastic modulus of Hawkesbury sandstone was a threshold value at 500°C, which explained the softening phenomenon of sandstone when the temperature exceeded 500°C. Lei et al. [34] used the MTS 815 MPa rock testing machine to monitor the microscopic failure process of sandstone during uniaxial compression testing. AE monitored the sandstone transition from brittleness to plasticity at approximately 600°C and found that the sandstone microscopic porosity decreased with increasing temperature. Mahanta et al. [35] conducted experiments on Manoharpur sandstone, Dholpur dolomite, and Bellary sandstone during these heating treatments. Their fracture strength increased by 40%, 25%, and 65%, respectively, within the range of 100°C. However, with temperature rising to 600°C, the fracture strength decreased by 59%, 36%, and 30%, respectively. Yang et al. [36] performed a dynamic compression test on

shale rocks and controlled the temperature between 20 and ~220°C. Their conclusion was that there was a temperature threshold between 20 and 220°C, before which the compressive strength increased with temperature and beyond which the compressive strength decreased with increasing temperature. Currently, many achievements have been made regarding the mechanical properties of rocks at diverse temperatures, dip angles, and confining pressures. They have mainly focused on the rupture modes of rocks at various temperatures. However, there have been few reports on the failure processes and acoustic emission characteristics under thermosolid coupling at different dip angles of shale bedding and thermosettings. Therefore, it is of great practical significance to carry out numerical simulation experiments to explore the mechanisms of thermosolid coupling on the propagation of shale fracturing and restructuring.

This paper utilizes the Lower Cambrian Niutitang Formation shale as the research object in the northern Guizhou area, uses statistical methods to describe the correlation between the bedding dip and temperature in the shale, and uses RFPA2D-Thermal to establish a numerical model of 5 groups of shale samples that have different dips. A constant confining pressure and several temperature conditions are set to simulate the natural environment of shale under high temperature and high pressure. Simultaneously, shale is analyzed in detail, in which the shale contains compressive strength and cracking processes at various temperatures, and the evolution of acoustic emission signals during the process is studied.

2. Geological Characteristics of the Study Area

2.1. Geographical Location of the Feng'gang No. 3 Block, South China. Guizhou is located in southwestern China and has unique geographic advantages in shale gas storage. Most areas of Guizhou are within the tectonic unit of the Yangtze block, which is divided into four blocks. The third block of shale gas in Feng'gang, Guizhou (referred to as the research area in the text), is an important part of the national shale gas resource experiment, with abundant resources and a good geological environment. The geographic location of the study area is located in the southeastern part of Zunyi city in the northern part of Guizhou Province (see Figure 1). The administrative divisions are located in the subregions of Meitan County, Feng'gang County, and Sinan County of Tongren city and parts of Meitan-Feng'gang-Tongren Sinan County from Zhengjiashan in Sinan County to Zhangjiapo and Tianjiawan Line in the east, Liujiawuji-Liangshuijing-Huangnipo Line in Meitan County in the west, Jiangjiagou-Ranjiayuanzi-Houtang Line in Tan County, Meitan County in the south, and North to Feng'gang Xianglu Mountain-Qinggang Park-Loquat Bay line. The area coverage in the study area is approximately 1167.49 km². The study area has diverse terrain types that contain hills, midmountains, hills and dams interspersed with each other, and karst landforms with conventional landforms alternately spread in between. The terrain is generally mountainous and hilly. The western terrain is dominated by flat dams and hills. Most areas contain
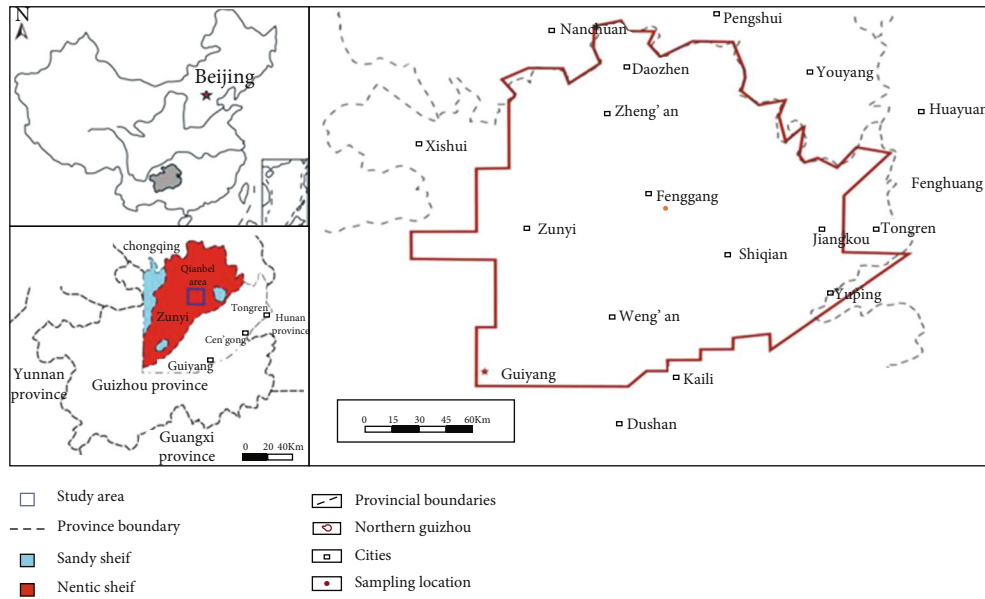
Figure 1: Detailed location map of the third district of the Feng'gang No. 3 block, Guizhou [37].

low hills and relatively flat valleys, with certain undulations. Some areas are cut by rivers (100~300 m), and the east is mountainous. The terrain is undulating, and the cut is deeper.

2.2. Influence of Folds and Fractures on Shale Temperature. The occurrence of folds and fractures caused the strata to no longer lie on the same plane during the same period, presenting a spatially scattered structure with a large depth decrease. Affected by structural compression and deformation, the Niutitang Formation in the study area is generally shallower in the southeast and northwest (approximately 1500 m and 500 m, respectively) and relatively deep in the middle (mainly 2000~4000 m); among them, the overall burial depth is between 1000 m and 3500 m, and the Meitan compound anticline is relatively shallow, with a burial depth of 500 m to 1500 m, while the Yachuan compound syncline contains Triassic strata, and the burial depth is at a maximum of 5000 m (see Figure 2). Near the study area, detailed logging data record the burial depth of the Niutitang Formation shale. The Niutitang Formation, which is located in Songtao Wuluo well ZK408 in the eastern part of the survey area, is present at a depth of 616.90~640.80 m. In the Deye 1 well in the northern part of the study area, the floor depth of the Niutitang Formation is at 1661.66~1752.20 m. In the drilling record of Well Fengshen 1, the Niutitang Formation is approximately 2500 m underground in Liujiazhai Village, Dangwan Township, Feng'gang County. The temperature of the stratum increases as depth increases. According to valid statistics, every time the depth increases by 100 meters, the temperature increases by 3°. The temperature at the Niutitang Formation in the study area is approximately 45°C~120°C. The amount of methane adsorption is greater at low temperature and low pressure, and the amount of free methane at high temperature and high pressure is greater. To approximate these real conditions, this study is conducted from 30°C to 90°C.

2.3. Pore Characteristics of Shale. Nanoscale pores are prevalent in shales, but the connectivity between pores is negligible. Shale gas is mainly stored in the micropores of shale. The size and connectivity of pores have a large impact on the ability of shale to adsorb shale gas and its storage performance. The degree of pore development in shale determines the permeability of shale and the degree of gas reservoir storage. Using nuclear magnetic resonance (NMR) technology, the pores of 5 groups of samples in the rock reservoirs in the study area are quantitatively tested, and the pore throat and pore size distributions are obtained [37].

Figure 3 shows that the pore throat and pore size distribution of each group of samples are approximately similar. Three peaks appear in the pore size distribution, indicating that the pore size range of shale is primarily concentrated at 0.001~0.1 μm and 0.01~0.4 μm, and a very small amount is distributed at 1~10 μm.

Through NMR analysis of the Lower Cambrian shale in the Feng'gang No. 3 block, it can be seen that the development of pores in the Lower Cambrian shale is advantageous to the storage of shale gas. This indicates that the development of shale gas in this area is economically important. It can also be seen from Figure 3 that although the micronscale pores are well developed, the connectivity between the pores is not good, and increasing the temperature helps to increase the porosity and permeability of the shale. It is therefore important to study the mechanism of damage under thermosolid coupling for the extraction of shale gas.

3. Thermosolid Coupling Element Model

3.1. Element Thermal Damage Evolutionary Theory. At the microscopic scale of shale, an element is considered to be an elastic body at the initial failure stage, and the stress-strain curve of each element is linear. When the damage threshold is reached, the properties of the unit begin to change. When shale is compressed, stretched, or sheared,
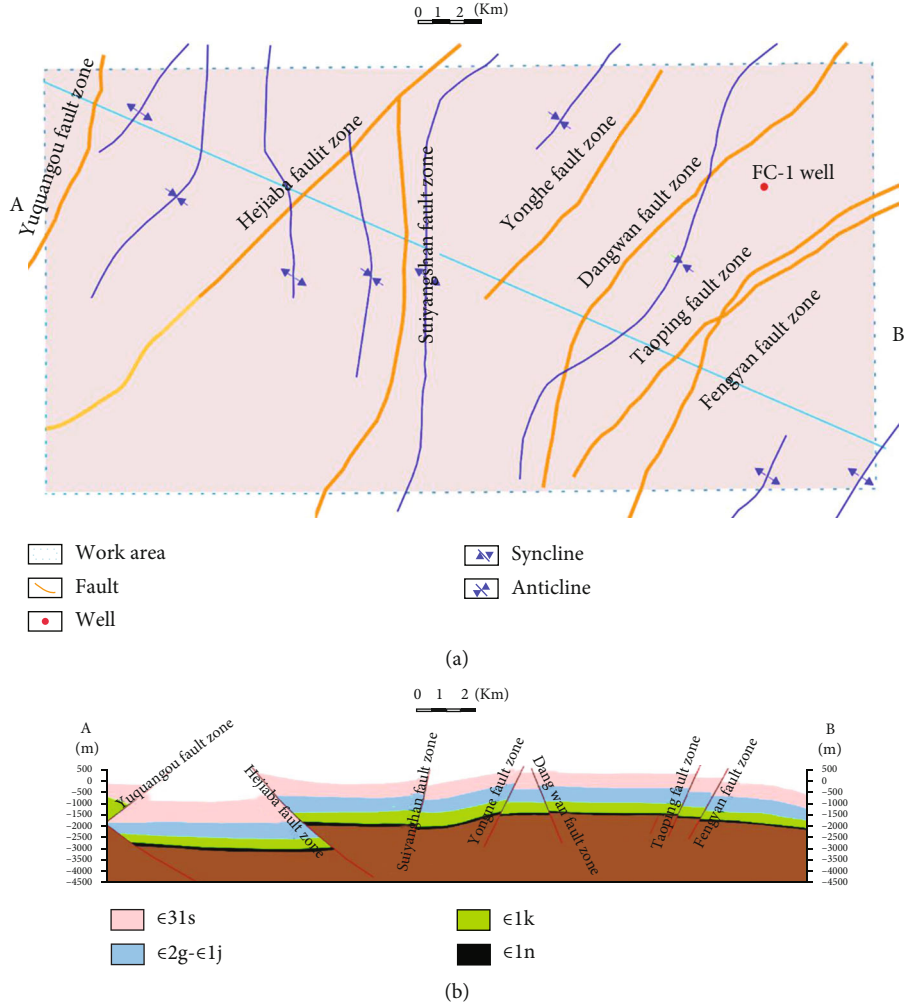
FIGURE 2: Geological formations in the study area. (a) Geological structural section view of the Feng'gang No. 3 block. (b) Basic structural feature map of the Feng'gang No. 3 block [37].

the tensile strength of shale is much smaller than the compressive strength, and tensile failure occurs, as shown in Equation (1). When shale reaches a critical state of stress, the shear stress exceeds the shear strength, and shear failure occurs, as shown in Equation (2) [38, 39].

$$F_1 \equiv \sigma_1 - f_{t0} = 0, \tag{1}$$

$$F_2 \equiv -\sigma_3 - \frac{1 + \sin \varphi}{1 - \sin \varphi} \sigma_1 - f_{c0} = 0. \tag{2}$$

F_1 and F_2 are the two damage threshold functions, and σ_1 and σ_3 are the maximum principal stress and minimum principal stress, respectively. In terms of the sign, the compressive stress is positive, and the tensile stress is negative. In actual situations, f_{t0} in the formula is expressed in terms of uniaxial tensile strength. f_{c0} is the uniaxial compressive strength of shale, and φ is the internal friction angle of the material. In the case of uniaxial compression and uniaxial tension, $f_{c0/}f_{c0} = f_{c0}/f_{c0} = \lambda$ indicates that the formula is applicable.

3.2. Element Thermosolid Coupling Equation. Assuming that the shale is an elastic body, the constitutive relationship satisfies the generalized Hooke's law. The shale in the study area is at high temperature and high pressure. Under this condition, Wee et al. proposed that the relationship between temperature variables and shale under combined loading is expressed as follows [40]:

$$\sigma'_{ij} = 2G\left(\varepsilon_{ij} + \delta_{ij} \frac{\nu}{1 - 2\nu} \varepsilon_{kk}\right) - K'\alpha_T T\delta_{ij}. \tag{3}$$

$\sigma'_{ij} = \sigma_{ij} + \xi p\delta_{ij}$, δ represents the total stress tensor (symbol is positive for tension), δ_{ij} is the Kronecker symbol, G is the shear modulus of the material, ν is Poisson's ratio, $\xi(\leq 1)$ is the compressibility of the material [$\xi = 1 - (K'/K_S)$], K_S is the shale material modulus of elasticity, and α is the volume expansion coefficient (K^{-1}). In this formula, the strain and stress caused by temperature changes are relative to the initial temperature; therefore, T is the temperature increase compared with the initial temperature.
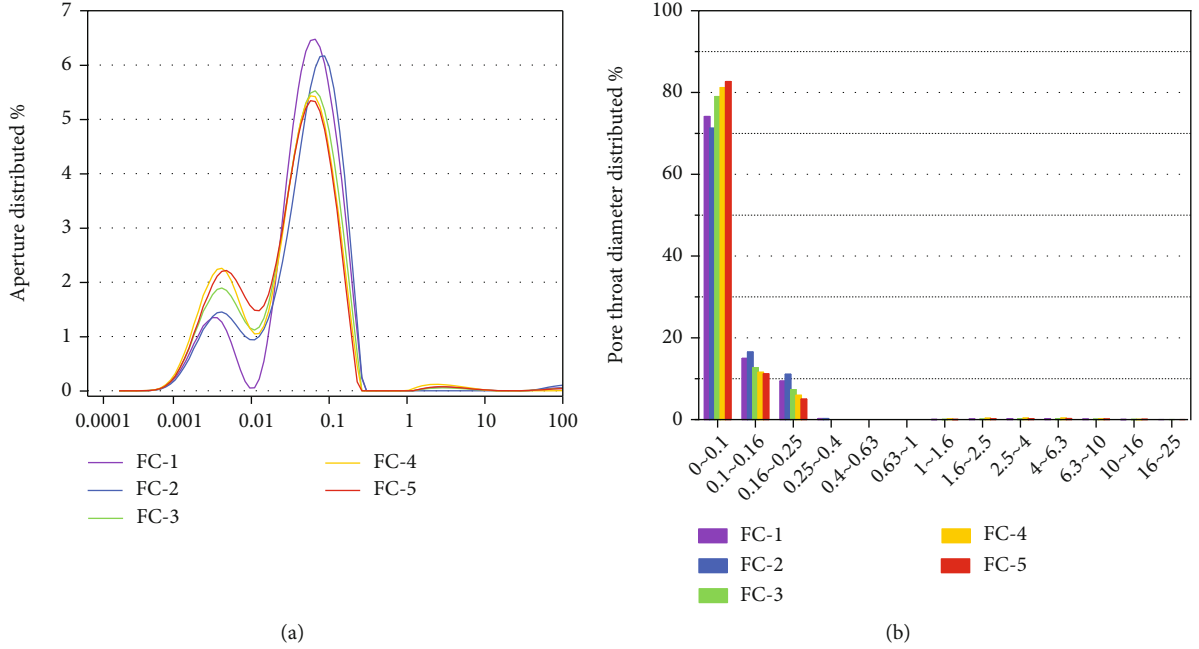
(a)

(b)

FIGURE 3: Distribution of pore size and pore throats. (a) Schematic diagram of shale aperture distribution/μm. (b) Pore throat diameter/μm [37].

During the research process, the interaction between mechanical energy and thermal energy is ignored. Based on the REV heat balance equation, it can be expressed as follows [26]:

$$(\rho_s C_s) \frac{\partial T}{\partial t} + (T_0 + T) K' \alpha_T \frac{\partial \varepsilon_v}{\partial t} = \lambda_s \nabla^2 T. \qquad (4)$$

In this formula, T_0 is the initial temperature (K) in the unstressed state, ρ_s is the density of the shale (kg/m^3), C_s is the specific heat capacity (J/kg·K), and λ_s is the heat transfer coefficient H of the shale (J/s·m·K). Equations (3) and (4) are a set of fully coupled nonlinear equations that control the thermosolid coupling of shale. This equation explains the evolution of heat transfer, compressibility, and thermal damage between shale materials under thermosolid coupling. The nonlinear differential equation is controlled by the second-order space partial derivative and the first-order time partial derivative. The nonlinear differential equation in the space and time domains is unsolvable.

3.3. Numerical Simulation. The RFPA temperature version software is used to study crack propagation under the thermosolid coupling of shale. RFPA is software that is based on the finite element, statistical damage theory, and Coulomb failure criterion. The deformation and failure of the rock are analyzed to obtain the true failure mode. This calculation method considers fully the randomness of the material distribution, such as rock heterogeneity and pores, and combines it with the statistical distribution assumption of material properties into the finite element algorithm. The division unit meets the given strength criterion; therefore, the rock under real conditions and the destruction process

can be presented through numerical simulation. In actual situations, many difficult-to-implement problems can be solved. Figure 4 shows the schematic diagram of controlling the displacement of the model with bedding inclinations of 0°~90°.

The discretization unit of RFPA obeys the Weibull distribution. On this premise, the relationship between the microscopic conditions and the mechanical properties of the macroscopic medium is established, and the Weibull statistical distribution function is introduced to describe the following [41]:

$$\varphi(\alpha) = \frac{m}{\alpha_0} \cdot \left(\frac{\alpha}{\alpha_0} \right)^{m-1} \cdot e^{-(\alpha/\alpha_0)^m}, \qquad (5)$$

where α is the mechanical property parameters of the primitive body, α_0 is the average value of the mechanical property parameters of the material, m is the parameter reflects the homogeneity of the material medium in a physical sense and is defined as the uniformity coefficient, and $\varphi(\alpha)$ is the statistical distribution density of the primitive property α.

In the RFPA temperature version, the temperature distribution function $T(x, y, z, t)$ is used to express the functional expression of the temperature change with time at each certain point in the rock.

In the calculation, the heat $q(x, y, z, t)$, $q = dQ/dt/S$, and Q per isothermal area are considered heat, t is time, and S is area, where q is proportional to the gradient of temperature function u, and the proportional coefficient H is the thermal conductivity.
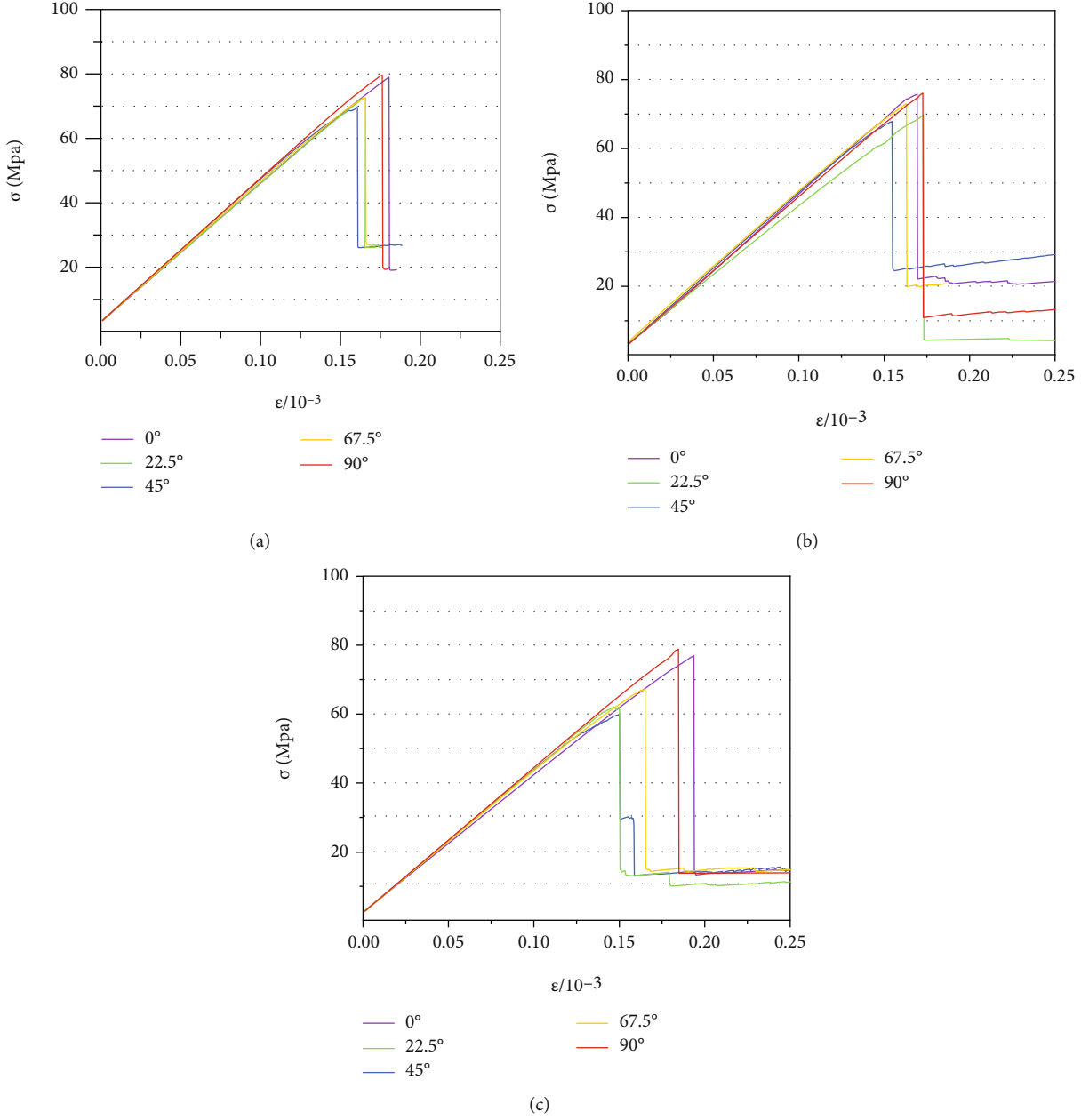
$$q = -k\nabla T \qquad (6)$$

(a)

(b)

(c)

FIGURE 4: Stress-strain curves of different bedding inclination angles at (a) 30°C, (b) 60°C, and (c) 90°C.

TABLE 1: Numerical simulation parameters [24].

Material	Elastic modulus/ MPa	Mean degree	Compressive strength/MPa	Poisson ratio ν	Internal friction angle (°)	Compression tension ratio	Thermal capacity	Thermal expansion coefficient	Heat transfer coefficient
Shale substrate	51600	4	145	0.22	35	14	3.250	1.36	0.20
Bedding	30960	2	116	0.31	30	13	2.153	1.30	3.57

The numerical experimental model uses a two-dimensional model to simulate shale at different temperatures. The calculation range is 100 mm in width and 100 mm in height. The entire numerical simulation model is divided into 100×100 units, and the initial value of displacement is set to 0.001 mm. The loading method is displacement loading $\Delta S = 0.0003$ mm and fixed confining pressure $p_1 = 10$ MPa. A layered structure with a thickness of 3 mm and a spacing of
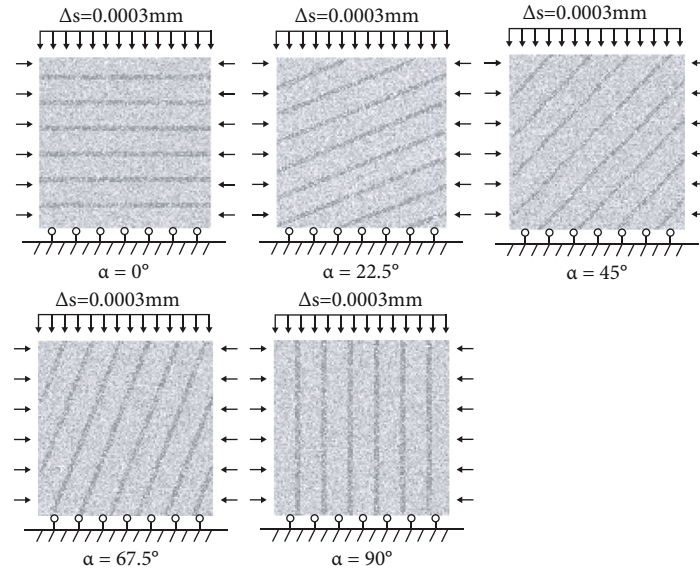
FIGURE 5: Schematic diagram of model loading.

15 mm is established in the model to simulate the layered structure of shale. The specific parameters in the model are shown (see Table 1) below.

The experimental study is a numerical model of shale with different bedding angles under the condition of gradually increasing temperature. The bedding angles in the model are set to 0°, 22.5°, 45°, 67.5°, and 90°. A schematic diagram of the model's overall conditions is shown in Figure 5. The fixed temperatures for the shale numerical model are 30°C, 60°C, and 90°C. The temperature boundary condition is set as the first type boundary condition (temperature is constant at 30°C, 60°C, and 90°C), and there is no heat flow between the shale matrix and outside world.

4. Analysis of Results

4.1. Analysis of Mechanical Characteristics of Shale Rupture. Figure 4 shows the stress-strain curves for shale at 30°C and dip angles of 0°, 22.5°, 45°, 67.5°, and 90° in a and 60°C and 90°C in (b) and (c). As seen from the graphs, the corresponding stress-strain curves for the shale change significantly with different inclinations, with temperature having less influence on the stress-strain curve than the effect of shale inclination. The damage of shale is broadly divided into four stages: the linear elastic stage, yielding stage, damage stage, and stability stage.

(1) The first stage is the linear elastic stage. In this stage, stress and strain have a linear relationship and exhibit good elastic properties. As seen in Figure 4, the linear elastic phase of the shale decreases significantly with increasing temperature and laminar dip angles of 22.5° and 45°. This indicates that the increase in thermal stress within the shale reduces the cementation between the shale matrix and laminae, and the softening effect becomes more pronounced as the lamina dip angle increases

(2) In the second stage of the yielding stage, influenced by the surrounding pressure and thermal stress, the temperature increase causes plastic deformation within the shale, and the shale stress-strain curve under the effect of thermosolid coupling shows a more obvious yielding stage

(3) The third stage is the failure stage. When the strength reaches its peak, the stress decreases sharply, and shale damage occurs. The graph shows that the failure strength of the shale decreases to a certain extent at each laminar dip angle after the temperature rises, especially at laminar dips of 22.5° and 45°. When the dip of the shale is the same and is accompanied by a decrease in temperature, the reduction in peak strength is due to the difference in the coefficient of thermal expansion between the bedding and shale matrix within the shale. When the particles are heated, they cause uneven expansion and uneven deformation of the shale. The particles squeeze each other so that a temperature-induced thermal stress is developed in the shale. As the temperature increases, the thermal stresses increase, resulting in thermal damage to the shale. More microfractures or primary fractures appear in the shale. On a macroscopic scale, the temperature of the shale increases. In this case, the strength decreases, which is consistent with the results of Yan et al., who studied mudstones [42]

(4) The fourth stage is the stabilization stage, where the tail end of the curve is smoothed. It can be seen from the graph that the stabilization phase at 30°C is shorter than that at 60°C and 90°C. At a temperature of 30°C, the damage mode of the shale mainly shows a brittle damage state. As the temperature increases, the properties of the shale change from brittle to plastic, showing an increase in the stability phase

Table 2: Simulation results of shale compressive strength.

Azimuth/ (°)	$t = 30°C$, compressive strength	$t = 60°C$, compressive strength	$t = 90°C$, compressive strength
0	78.98	75.81	76.91
22.5	72.69	68.67	62.34
45	69.64	67.79	59.79
67.5	72.65	72.86	67.20
90	79.61	74.98	78.79

Table 3: The bedding effect coefficient of the compressive strength of shale.

Azimuth/ (°)	$t = 30°C$, bedding effect coefficient	$t = 60°C$, bedding effect coefficient	$t = 90°C$, bedding effect coefficient
0	0	0	0
22.5	0.01	0.08	0.25
45	0.12	0.11	0.22
67.5	0.08	0.04	0.13
90	-0.01	0.01	-0.02

Figure 6: Shale peak intensity variation law.
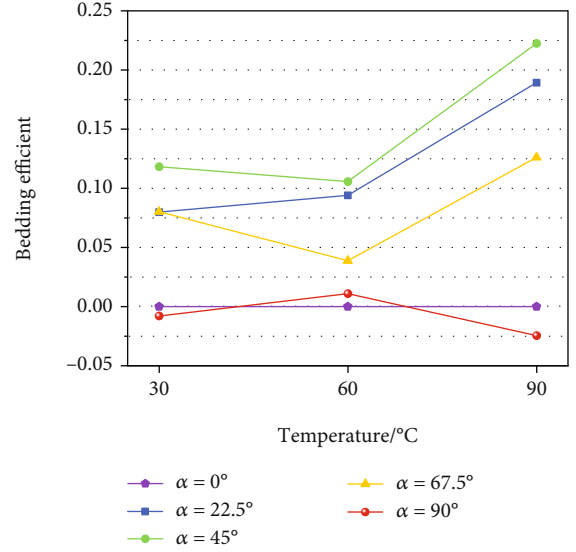
Figure 7: Variation law of the shale bedding effect at different temperatures and different dip angles.
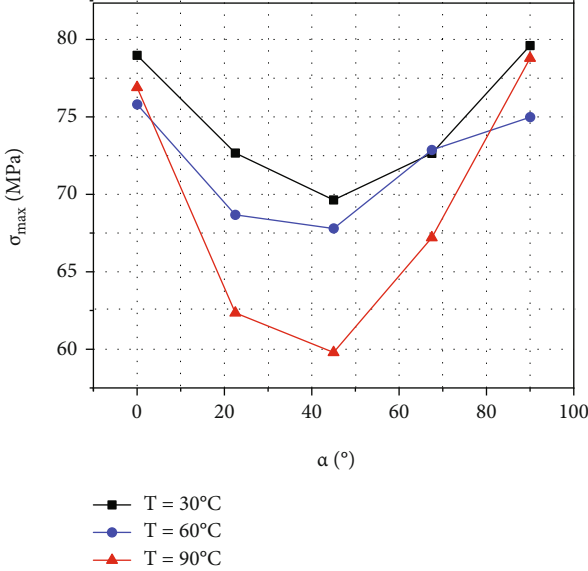
Table 2 shows the compressive strength of shale with different bedding dip angles obtained by numerical simulation at 30°C, 60°C, and 90°C. The compressive strengths from Table 2 are plotted in Figure 6, from which it can be seen that the compressive strength of the shale reaches its maximum at 30°C, while the compressive strength decreases with increasing temperature. Additionally, temperature has a strong effect on the anisotropy of shale bedding, with increasing temperature leading to reduced cementation of the laminae to the shale matrix, and the effect is strongest at lamina dips of 22.5° and 45°. At temperatures of 30°C and 60°C, the compressive strength of the bedding inclination is greatest at 0° and least at 45°. As the azimuth of the bedding rises, the compressive strength of the shale shows a trend of first falling and then rising. When the temperature is 90°C, the compressive strength is greatest at a bedding azimuth of 90°. Alternatively, the compressive strength is lowest at 45° because of the weak cementation between the shale matrix and weak bedding surface. As the temperature increases, the thermal stress resulting from the incompatible expansion of the laminated particles and shale matrix gradually increases, and the compressive strength of the shale specimens decreases under the combined effect of the thermal stress and lamination effect.

As seen from the variation curve in Figure 6, the encrusted shale exhibits a strong lamina effect. To represent the effect of laminations on the mechanical properties of shale under thermosolid coupling, $S(\alpha)$ is used to characterize the structural effect of the laminations. The bedding effect is 1 minus the compressive strength at different inclination angles divided by the compressive strength measured at the inclination level. The expression is as follows [24]:

$$S(\alpha) = 1 - \frac{\theta(\alpha)}{\theta(0°)}. \tag{7}$$

In the formula, $S(\alpha)$ is the bedding effect coefficient, $\theta(\alpha)$ is the compressive strength of different bedding dips, and $\theta(0°)$ is the compressive strength of the shale when the bedding dip is 0°. According to the above formula, Table 3 shows the bedding effect coefficients of different shale dip angles. To observe the changes in bedding effect coefficients more intuitively, bedding effect diagrams of different bedding dip angles at 30°C, 60°C, and 90°C are drawn.

As shown in Figure 7, the shale lamina effect rises more slowly at 60°C with increasing temperature, with a significant effect at 90°C. The laminar effect is not evident for dips of 0° versus 90°, and temperature changes within 30°C to
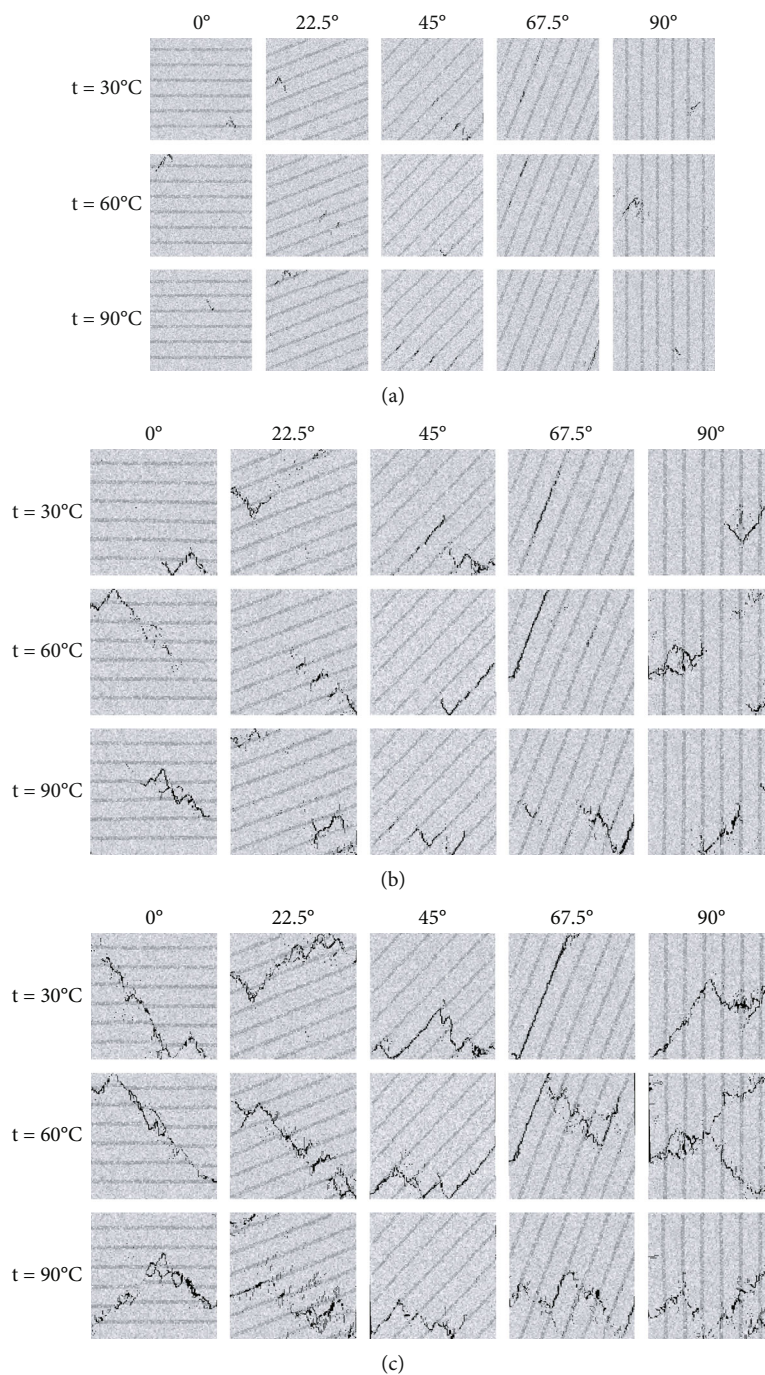
(a)
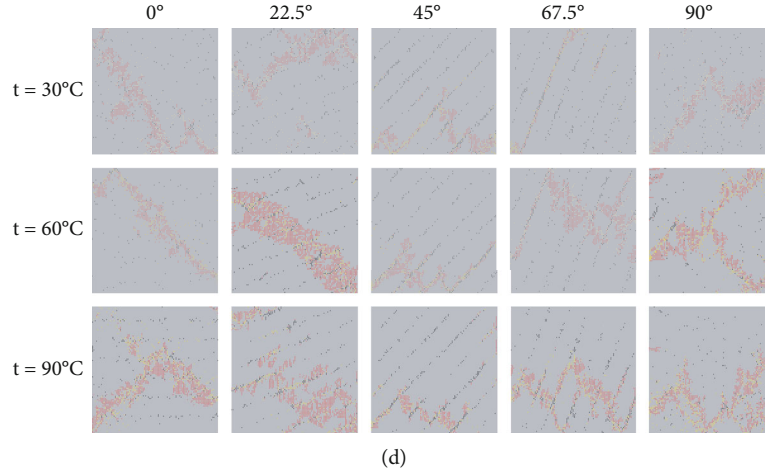

(b)

(c)

Figure 8: Continued.

(d)

FIGURE 8: Fracture process and acoustic emission diagram of shale. (a) Crack initiation. (b) Crack propagation. (c) Instability mode. (d) Acoustic emission.

TABLE 4: Fractal dimensions at different temperatures and stress levels.

Stress level azimuth		10%	20%	30%	40%	50%	60%	70%	80%	90%	100%	Temperature
	D_s	0	0	0	0	0.129	0.278	0.411	0.572	0.771	0.978	30°C
0°	D_s	0	0	0	0	0.109	0.254	0.352	0.522	0.714	0.897	60°C
	D_s	0	0	0	0	0.327	0.532	0.667	0.796	0.916	1.063	90°C
	D_s	0	0	0	0	0.303	0.413	0.557	0.731	0.849	1.057	30°C
22.5°	D_s	0	0	0	0.231	0.385	0.551	0.717	0.82	0.916	1.091	60°C
	D_s	0	0	0	0	0.341	0.492	0.656	0.819	0.906	1.269	90°C
	D_s	0	0	0	0	0.128	0.451	0.626	0.769	0.872	1.037	30°C
45°	D_s	0	0	0	0	0.280	0.417	0.593	0.743	0.870	1.018	60°C
	D_s	0	0	0	0	0.261	0.461	0.609	0.720	0.874	1.1	90°C
	D_s	0	0	0	0	0.241	0.419	0.554	0.756	0.837	0.874	30°C
67.5°	D_s	0	0	0	0	0	0.409	0.575	0.719	0.852	0.977	60°C
	D_s	0	0	0	0	0.297	0.437	0.565	0.731	0.909	1.079	90°C
	D_s	0	0	0	0	0	0.054	0.520	0.631	0.772	0.897	30°C
90°	D_s	0	0	0	0	0	0.600	0.662	0.782	0.940	1.179	60°C
	D_s	0	0	0	0	0	0	0.428	0.591	0.734	1.286	90°C

90°C have little effect on the strength of the units divided within the shale, in the form of a smooth curve in the graph. The laminar effect curves for the 22.5°, 45°, and 67.5° shale specimens show a decreasing and then increasing pattern. The temperature rises to 90°C, the thermal stress from the uneven expansion of the particles within the shale rises sharply, and the shale matrix turns to plastic deformation between the shale and laminae, leading to a weakening of cementation; therefore, the lamina effect increases, and the fold line in the diagram shows a rapid rise.

4.2. Failure and Deformation Characteristics of Shale under Thermosolid Coupling. During the evolution of shale damage by thermosolid coupling, shale specimens reach peak strength followed by a sharp decrease in stress and sudden rupture. Figure 8 shows the damage process and the corresponding acoustic emission variation pattern for shales with different bedding dips at a fixed confining pressure. As seen from the diagram, the shale undergoes three stages: fracture initiation, fracture extension, and penetration. Figure 8(a) shows the fracture initiation phase of the shale damage process, Figure 8(b) shows the fracture extension and expansion phase, Figure 8(c) shows the final destabilization damage phase, and Figure 8(d) shows the acoustic emission map corresponding to the damage phase, where red represents tensile damage, yellow is shear damage, and the black area is the damaged unit. As seen in Figure 8(c), the damage pattern is significantly influenced by the lamination effect,
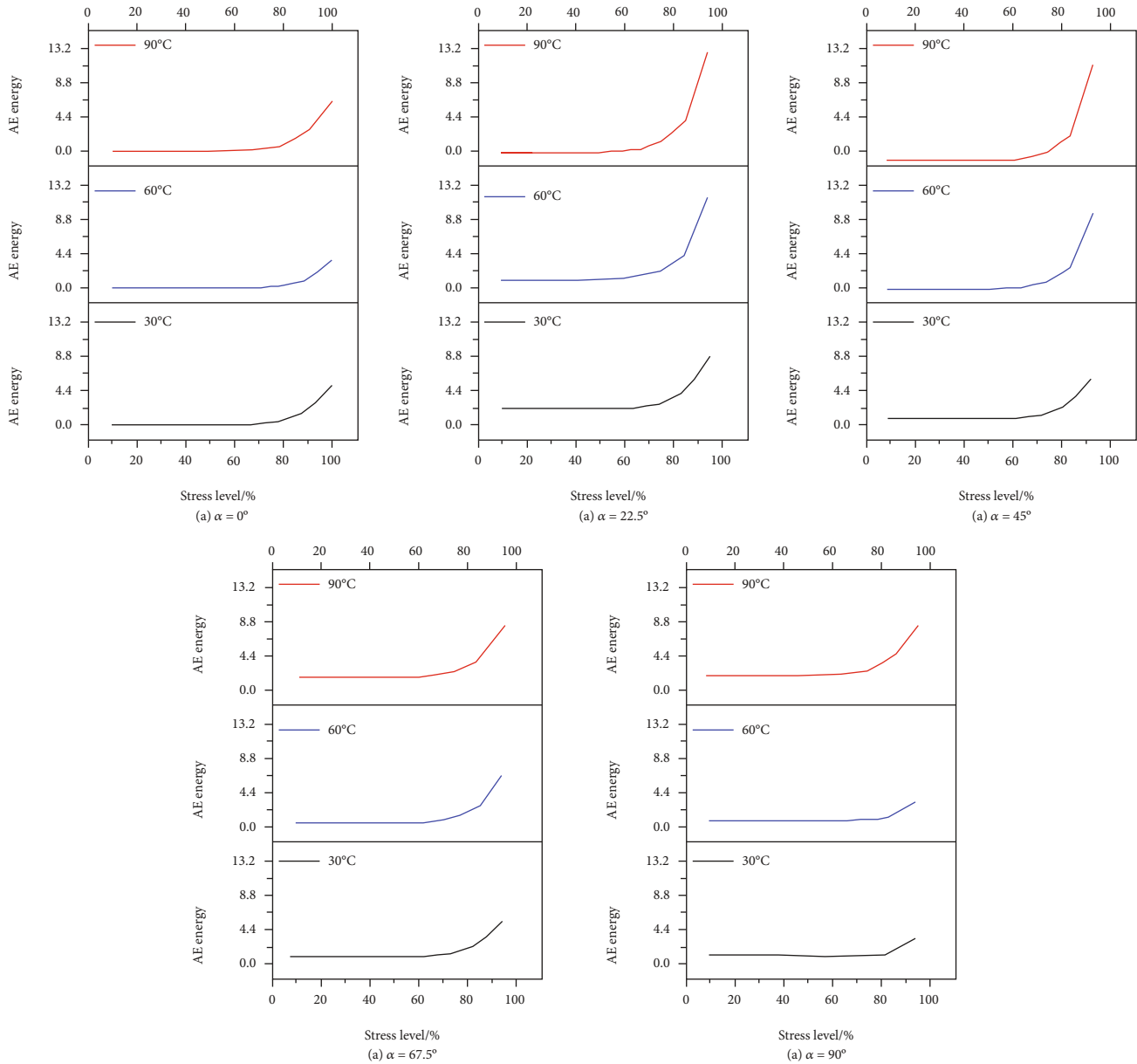
FIGURE 9: Plot of AE energy versus temperature and stress level.

with an increase in temperature having a definite effect on the change in damage pattern. The damage patterns of shales with different laminar dips at the three temperatures are classified into five damage patterns.

(1) *N-type ($90°_{30°C}$, $67.5°_{60°C}$, $90°_{60°C}$, and $45°_{90°C}$).* During the evolution of fractures in these groups of shale specimens, cracks first appear in the laminae. As loading progresses, the cracks extend through the laminae and eventually penetrate the shale matrix along a 45° or 135° dip to form an N-fracture. When the laminar inclination is at a high angle, temperatures below 60°C have less effect on the damage pattern, and temperatures of 90°C strengthen the laminar effect. The lamina effect is stronger at high

angular lamina dips, and the laminae have a strong dominant effect on the overall shale integrity. As seen from the acoustic emission diagrams in Figure 8(d), these shale specimens are mainly distributed in tensile stresses during the final damage phase, but there are a number of shear stresses in the laminae, which can be judged to be a gradual increase in tensile stresses in the shale matrix after shear damage has occurred in the laminae.

(2) ⊠-type ($45°_{30°C}$ and $0°_{90°C}$). In both groups, the shale with a laminar dip of 45° at a temperature of 30°C cracks first in the laminae during damage, showing a strong lamina effect. In contrast, shales with a laminar dip of 0° at 90°C are cracked first in the shale

(a) $\alpha = 0°$

(a) $\alpha = 22.5°$

(a) $\alpha = 45°$

(a) $\alpha = 67.5°$
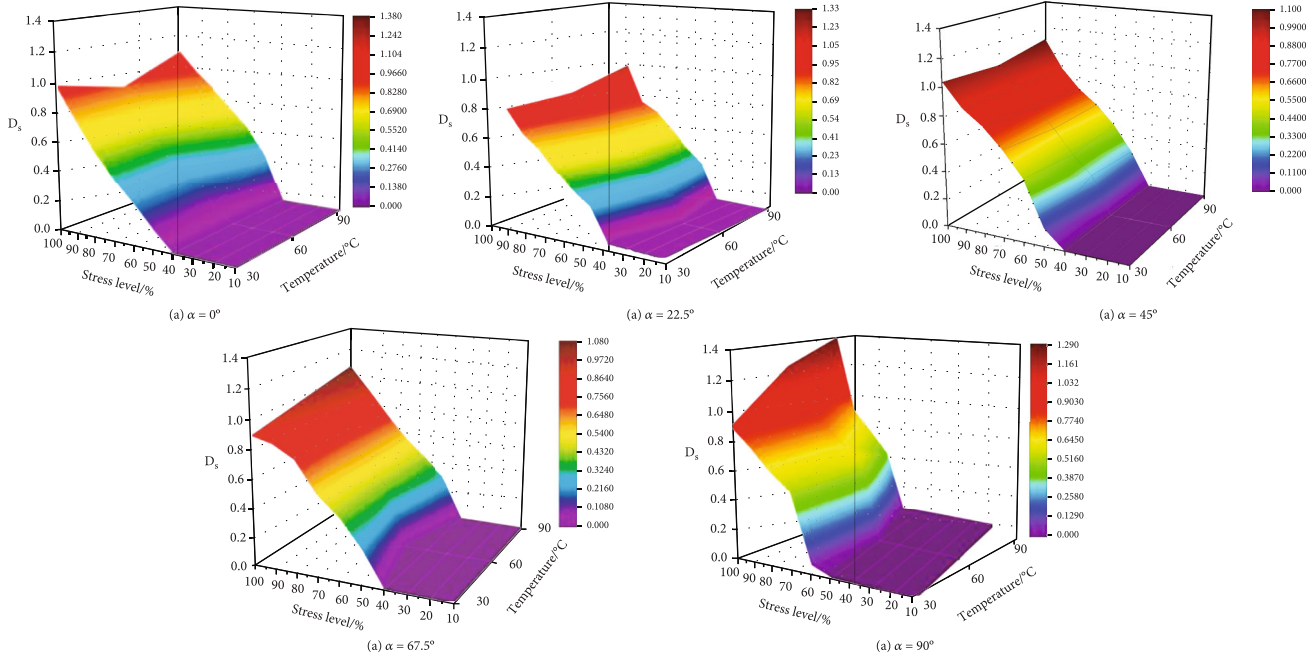

(a) $\alpha = 90°$

FIGURE 10: Relationships between different temperatures, stress levels, and fractal dimensions.

matrix, at which point the temperature effect manifests itself significantly. Shear damage occurs in the lamina section at a lamina dip of 45°, as seen in Figure 8(d), while shear damage occurs within the shale matrix at a lamina dip of 0°.

(3) *v-type ($22.5°_{30°C}$ and $45°_{60°C}$)*. Shale specimens with a laminar dip angle of 22.5° at a temperature of 30°C show internal cracks in both the shale matrix and laminae, eventually forming v-shaped cracks along the laminae. Specimens with a lamina dip angle of 45° at a temperature of 60°C show a strong lamina effect, with cracks appearing in the lamina and then breaking along the lamina.

(4) *Slanted I-type ($0°_{30°C}$, $67.5°_{30°C}$, $0°_{60°C}$, and $22.5°_{60°C}$)*. Damage to shale specimens at low laminar angles is primarily subject to tensile and shear stresses, when the surrounding pressure plays a major factor in preventing multiple cracks from forming. The specimen with a high angle of 67.5° at a temperature of 30°C is then subject to the effects of perimeter pressure and laminae, with cracks expanding along the laminae and the perimeter pressure preventing the formation of multiple cracks, resulting in an oblique I-shaped damage pattern.

(5) *Cluttered-type ($22.5°_{90°C}$, $67.5°_{90°C}$, and $90°_{90°C}$)*. At the higher temperatures of the 90°C complex, irregular disorganized damage is more likely to occur. At a temperature of 90°C, the laminar and temperature effects of the shale reach their maximum at the same time, and thermal and loading stresses within the shale act together to cause the shale to exhibit a complex damage pattern.

According to the above analysis, the surrounding pressure at low angles of the shale laminae is the dominant factor in the damage pattern with simpler forms of damage and more complex damage occurring as the temperature rises. The lamina effect is stronger at high angles in shale laminae, where the lamina effect is the main controlling factor, mainly manifesting itself as damage occurring first along the laminae, with the lamina effect acting in conjunction with the temperature effect to produce a more complex damage pattern as the temperature rises. During hydraulic fracturing, hydraulic fractures may extend along high angular laminar dips, inhibiting the expansion of the fracture network, while higher temperatures contribute to the formation of complex fracture networks, thereby increasing shale gas production.

4.3. Quantitative Fractal Characterization of Shale Damage under Thermosolid Coupling. Analytical theory can be used to quantitatively describe irregular and complex matters in nature, including the evolution of damage to rocks. Shale converts its internal stored energy into elastic waves and releases them rapidly at the moment of destruction, a phenomenon known as acoustic emission [43, 44]. During shale damage, acoustic emission occurs for each unit that breaks down; therefore, acoustic emission has a fractal character. In this paper, images of acoustic emissions at different stress levels are grayed out by ImageJ and imported into a MATLAB calculation program to find their fractal dimension. The fractal dimension is solved by the following [45]:

$$D_s = -\lim_{1/r \longrightarrow 0} \frac{\log N(r)}{\log 1/r}, \tag{8}$$

where D_s is the adaptive fractal dimension of the damaged

region, r is the side length of the square box, and $N(r)$ is the number of square boxes with side length r needed to cover the damaged region therein.

Table 4 shows the fractal dimension values. Figures 9 and 10 show the trends between AE energy, fractal dimension, laminar dip, temperature, and stress level. As shown in Figure 9, the AE energy generally shows an increase with increasing stress levels. At stress levels less than 50%, the AE energy of each group is almost zero, showing little or no damage. When the stress level is between 50% and 80%, the AE energy rises slowly at this stage, with a more pronounced rise in AE energy in low-angle shale specimens compared with high-angle shale. When stress levels exceed 80%, AE energy rises rapidly, and shale damage breaks down. 22.5°, 45°, and 67.5° show significant increases in AE energy, corresponding to the macroscopic damage forms, with high release energy representing intense shale damage and injury. An increase in energy is observed as the temperature rises, at which point the macroscopic damage intensifies, with an insignificant increase in energy at 60°C and a significant increase at 90°C, when the corresponding damage pattern becomes more complex. Figure 10 shows the fractal dimension as a function of laminar dip, temperature, and stress level, with the x-axis coordinates representing stress level and the y-axis coordinates representing temperature. It is clear from the graphs that the fractal dimension generally increases with increasing temperature, and at $\alpha = 22.5°$, 67.5°, and 90°, the fractal dimension increases more with increasing temperature, indicating that temperature enhances the laminar effect of the three groups of shale dip specimens, and the macroscopic phenomenon shifts from simple oblique I or N damage to more complex heterogeneous damage. Conversely, smaller fractal dimensions correspond to simpler forms of destruction.

5. Conclusion

In this paper, the effect of temperature on the damage process of shales containing laminated shales with different dip angles is studied by establishing a coupled thermosolid model for shales of the Niutitang Formation, and the following laws are summarized:

(1) The temperature increase reduced the linear elastic phase of the shale specimens in each group, with a significant reduction in the linear elastic phase of shales with lamina dip angles of 22.5° and 45°. The elevated temperature causes partial plastic deformation within the shale, and the shale stress-strain curve under thermosolid coupling exhibits a more pronounced yielding phase

(2) When the temperature rises from 30°C to 60°C, it makes the unit swell leading to an increase in pore space, which further compacts the shale matrix with the laminae under displacement-controlled loading, and the lamina effect decreases to a small extent. And after the temperature reaches 90°C, the thermal stress generated by the uneven expansion of particles inside the shale rises sharply. The shale matrix and laminae turn to plastic deformation between them leading to weakening of cementation, and the strengthening effect of laminae in shale is most significant

(3) The shale damage patterns are grouped into five categories (N-Type, ∧-Type, v-type, slanted I-type, and cluttered-type). Among them, the occurrence of N-type damage is mainly due to the strong dominant effect of high-angle laminae on the integrity of the whole shale, and the warming reinforces the lamina effect. The ∧ and v shapes mainly occur when the dip angle of the laminae is 45°. The sloping I-shaped damage occurs in shale specimens with low laminar dip, which are mainly subjected to tensile and shear stresses, when the surrounding pressure plays a major role in preventing the formation of multiple cracks. Heterogeneous damage occurs at a temperature of 90°C. The lamina effect and temperature effect of the shale reach a maximum at the same time, and the thermal and loading stresses inside the shale act together to give the shale a complex damage pattern

(4) The active role of temperature in shale damage is further quantified by the fractal dimension. The fractal dimension curve is relatively flat when the temperature is 60°C, while the fractal dimension rises rapidly by 90°C, indicating that the fractal extension of the shale is most favorable at a temperature of 90°C. At $\alpha = 22.5$, 67.5°, and 90°, the fractal dimension increases with increasing temperature, indicating that the laminar effect of the three groups of shale dip specimens is strongly influenced by temperature, and the macroscopic phenomenon shifts from simple oblique I- or N-shaped damage to more complex heterogeneous damage

Data Availability

The data used to support the study is available within the article.

Conflicts of Interest

The authors declare that they have no conflicts of interest.

Acknowledgments

References

[1] J. Cooper, L. Stamford, and A. Azapagic, "Environmental impacts of shale gas in the UK: current situation and future scenarios," *Energy Technology*, vol. 2, no. 12, pp. 1012–1026, 2015.

[2] L. E. William, "Impacts of shale gas advancements on natural gas utilization in the United States," *Energy Technology*, vol. 2, no. 12, pp. 953–967, 2014.

[3] M. Zhang, W. Guo, and Z. Lei, "Patent analysis of shale gas technology in China and implications for its exploitation," *Energy Technology*, vol. 2, no. 12, pp. 1040–1045, 2015.

[4] S. S. Zhiltsov and I. S. Zonn, "Shale Gas Production in the USA," in *Shale gas: Ecology, politics, economy*, pp. 25–35, Springer, Cham, 2016.

[5] J. Cooper, L. Stamford, and A. Azapagic, "Shale gas: a review of the economic, environmental, and social sustainability," *Energy Technology*, vol. 4, no. 7, pp. 772–792, 2016.

[6] Y. Wang, Y. Zhu, S. Chen, and W. Li, "Characteristics of the nanoscale pore structure in Northwestern Hunan shale gas reservoirs using field emission scanning electron microscopy, high-pressure mercury intrusion, and gas adsorption," *Energy Fuels*, vol. 28, no. 2, pp. 945–955, 2014.

[7] L. Wang, Y. Guo, C. Yang, J. Xiao, C. Lu, and Y. Song, "Mechanical characterization of continental shale in Sichuan Basin of China and its potential impact on reservoir stimulation," *Journal of Natural Gas Science and Engineering*, vol. 79, p. 103346, 2020.

[8] Z. Li, S. Liu, W. Ren, J. Fang, and Z. Dun, "Multiscale laboratory study and numerical analysis of water-weakening effect on shale," *Advances in Materials Science and Engineering*, vol. 2020, Article ID 5263431, 14 pages, 2020.

[9] L. Li, B. Huang, Y. Li, R. Hu, and X. Li, "Multi-scale modeling of shale laminas and fracture networks in the Yanchang formation, Southern Ordos Basin, China," *Engineering Geology*, vol. 243, pp. 231–240, 2018.

[10] J. Liu, W. Ding, R. Wang et al., "Quartz types in shale and their effect on geomechanical properties: an example from the Lower Cambrian Niutitang Formation in the Cen'gong block, South China," *Applied Clay Science*, vol. 163, pp. 100–107, 2018.

[11] H. Song, Z. Wu, A. Wang, W. Sun, and Y. Zuo, "Study on the microscale tensile properties of Lower Cambrian Niutitang Formation shale based on digital images," *Geofluids*, vol. 2020, Article ID 8828965, 14 pages, 2020.

[12] M. Tang, Z. Wu, A. Wang, Y. Zuo, and W. Sun, "Study on the microscopic fracture process and acoustic emission of shale based on digital image," *Geofluids*, vol. 2021, Article ID 8874918, 14 pages, 2021.

[13] Y. Wu and Y. Yang, "The competition situation analysis of shale gas industry in China: applying Porter's five forces and scenario model," *Renewable and Sustainable Energy Reviews*, vol. 40, pp. 798–805, 2014.

[14] R. Wang, Y. Gu, W. Ding et al., "Characteristics and dominant controlling factors of organic-rich marine shales with high thermal maturity: a case study of the Lower Cambrian Niutitang Formation in the Cen'gong block, southern China," *Journal of Natural Gas Science and Engineering*, vol. 33, pp. 81–96, 2016.

[15] W. Ju, C. Wu, and W. Sun, "Effects of mechanical layering on hydraulic fracturing in shale gas reservoirs based on numerical models," *Arabian Journal of Geosciences*, vol. 11, no. 12, 2018.

[16] M. M. Nezhad, Q. J. Fisher, E. Gironacci, and M. Rezania, "Experimental study and numerical modeling of fracture propagation in shale rocks during Brazilian disk test," *Rock Mechanics & Rock Engineering*, vol. 51, no. 6, pp. 1755–1775, 2018.

[17] Y. Wang, X. Li, Y. X. Zhang, Y. S. Wu, and B. Zheng, "Gas shale hydraulic fracturing: a numerical investigation of the fracturing network evolution in the Silurian Longmaxi formation in the southeast of Sichuan Basin, China, using a coupled FSD approach," *Environmental Earth Sciences*, vol. 75, no. 14, 2016.

[18] H. Cui, Z. Wu, L. Li, J. Wang, and Y. Lou, "Numerical test study of the microscale failure modes and fractal analysis of Lower Cambrian shale based on digital images," *Advances in Civil Engineering*, vol. 2020, Article ID 8819711, 16 pages, 2020.

[19] N. Shrestha, G. Chilkoor, J. Wilder, V. Gadhamshetty, and J. J. Stone, "Potential water resource impacts of hydraulic fracturing from unconventional oil production in the Bakken shale," *Water Research*, vol. 108, pp. 1–24, 2017.

[20] Z. Wu, H. Song, L. Li, Z. Zhou, and Y. Lou, "Study on the damage evolution process and fractal of quartz-filled shale under thermal-mechanical coupling," *Geofluids*, vol. 2021, Article ID 8843120, 14 pages, 2021.

[21] C. Qin, Y. Jiang, Y. Luo, J. Zhou, and Y. Xie, "Effect of supercritical CO2 saturation pressures and temperatures on the methane adsorption behaviours of Longmaxi shale," *Energy*, vol. 206, p. 118150, 2020.

[22] T. F. Rexer, M. J. Benham, A. C. Aplin, and K. M. Thomas, "Methane adsorption on shale under simulated geological temperature and pressure conditions," *Energy & Fuels*, vol. 27, no. 6, pp. 3099–3109, 2013.

[23] D. H. Johnston, "Physical properties of shale at temperature and pressure," *SEG Technical Program Expanded Abstracts*, vol. 4, no. 1, 2012.

[24] Y. Lou, Z. Wu, W. Sun et al., "Study on failure models and fractal characteristics of shale under seepage-stress coupling," *Energy Science & Engineering*, vol. 8, no. 5, pp. 1634–1649, 2020.

[25] C. H. Wei, W. C. Zhu, Q. L. Yu, T. Xu, and S. Jeon, "Numerical simulation of excavation damaged zone under coupled thermal- mechanical conditions with varying mechanical parameters," *International Journal of Rock Mechanics & Mining Sciences*, vol. 75, pp. 169–181, 2015.

[26] Y. Zhou, R. K. N. D. Rajapakse, and J. Graham, "A coupled thermoporoelastic model with thermo-osmosis and thermal-filtration," *International Journal of Solids & Structures*, vol. 35, no. 34-35, pp. 4659–4683, 1998.

[27] O. Alm, L. L. Jaktlund, and K. Shaoquan, "The influence of microcrack density on the elastic and fracture mechanical properties of Stripa granite," *Physics of the Earth and Planetary Interiors*, vol. 40, no. 3, pp. 161–179, 1985.

[28] B. M. Lu, B. L. Tian, W. J. Liang, and M. M. Hong, "Experimental study on the influence of temperature on shale mechanical properties under conventional triaxial compression," *Advanced Materials Research*, vol. 250-253, pp. 1452–1455, 2011.

[29] Z. Wang, J. Pan, Q. Hou, B. Yu, M. Li, and Q. Niu, "Anisotropic characteristics of low-rank coal fractures in the Fukang mining area, China," *Fuel*, vol. 211, pp. 182–193, 2018.

[30] G. Yao, Q. Chen, H. Liu, Y. Tan, and L. Wang, "Experimental study on mechanical properties of lower silurian longmaxi

formation laminated shale in Southeast Yu," *Journal of Rock Mechanics and Engineering*, vol. 34, no. S1, pp. 3313–3319, 2015.

[31] M. Masri, M. Sibai, J. F. Shao, and M. Mainguy, "Experimental investigation of the effect of temperature on the mechanical behavior of Tournemire shale," *International Journal of Rock Mechanics & Mining Sciences*, vol. 70, pp. 185–191, 2014.

[32] P. K. Gautam, A. K. Verma, S. Maheshwar, and T. N. Singh, "Thermomechanical analysis of different types of sandstone at elevated temperature," *Rock Mechanics & Rock Engineering*, vol. 49, no. 5, pp. 1985–1993, 2016.

[33] P. G. Ranjith, D. R. Viete, J. C. Bai, and M. Perera, "Transformation plasticity and the effect of temperature on the mechanical behaviour of Hawkesbury sandstone at atmospheric pressure," *Engineering Geology*, vol. 151, pp. 120–127, 2012.

[34] R. Lei, Y. Wang, L. Zhang, B. Liu, and Y. K. Wang, "The evolution of sandstone microstructure and mechanical properties with thermal damage," *Energy Science & Engineering*, vol. 7, no. 6, pp. 3058–3075, 2019.

[35] B. Mahanta, T. N. Singh, and P. G. Ranjith, "Influence of thermal treatment on mode I fracture toughness of certain Indian rocks," *Engineering Geology*, vol. 210, pp. 103–114, 2016.

[36] G. Yang, J. Liu, X. Li, and J. Bi, "Effect of temperature on shale strength under dynamic impact loading," *Arabian Journal of Geosciences*, vol. 13, no. 12, 2020.

[37] Z. Wu, Y. Zuo, S. Wang et al., "Numerical study of multi-period palaeotectonic stress fields in Lower Cambrian shale reservoirs and the prediction of fractures distribution: a case study of the Niutitang Formation in Feng'gang No. 3 block, South China," *Marine and Petroleum Geology*, vol. 80, pp. 369–381, 2017.

[38] W. C. Zhu and C. A. Tang, "Micromechanical model for simulating the fracture process of rock," *Rock Mechanics & Rock Engineering*, vol. 37, no. 1, pp. 25–56, 2004.

[39] W. C. Zhu, C. H. Wei, S. Li, J. Wei, and M. S. Zhang, "Numerical modeling on destress blasting in coal seam for enhancing gas drainage," *International Journal of Rock Mechanics and Mining Sciences*, vol. 59, pp. 179–190, 2013.

[40] A. Wcz, A. Chw, C. Jlb, B. Hyq, and D. De, "A model of coal—gas interaction under variable temperatures - ScienceDirect," *International Journal of Coal Geology*, vol. 86, no. 2-3, pp. 213–221, 2011.

[41] C. A. Tang, H. Liu, P. K. K. Lee, Y. Tsui, and L. G. Tham, "Numerical studies of the influence of microstructure on rock failure in uniaxial compression – part I: effect of heterogeneity," *International Journal of Rock Mechanics and Mining Sciences*, vol. 37, no. 4, pp. 555–569, 2000.

[42] S. X. Yan, X. L. Wang, and Z. G. Liu, "Experimental study on bedding structure effect in mudstone drilling," *Industrial Minerals & Processing*, vol. 46, pp. 59–62, 2017.

[43] H. P. Xie, J. F. Liu, Y. Ju, J. G. Li, and L. Z. Xie, "Fractal property of spatial distribution of acoustic emissions during the failure process of bedded rock salt," *International Journal of Rock Mechanics and Mining Sciences*, vol. 48, 2011.

[44] S. W. Zhang, K. J. Shou, X. F. Xian, J. P. Zhou, and G. J. Liu, "Fractal characteristics and acoustic emission of anisotropic shale in Brazilian tests," *Tunnelling and Underground Space Technology*, vol. 71, pp. 298–308, 2018.

[45] R. Zhang, F. Dai, M. Z. Gao, N. W. Xu, and C. P. Zhang, "Fractal analysis of acoustic emission during uniaxial and triaxial loading of rock," *International Journal of Rock Mechanics and Mining Sciences*, vol. 79, pp. 241–249, 2015.